Incipient plasticity of twin and stable/unstable grain boundaries during nanoindentation in copper

T. Tsuru,[1] Y. Kaji,[1] D. Matsunaka,[2] and Y. Shibutani[2]
[1]*Nuclear Science and Engineering Directorate, Japan Atomic Energy Agency, 2-4 Shirakata-Shirane, Tokai-mura, Ibaraki, Japan*
[2]*Department of Mechanical Engineering, Osaka University, 2-1 Yamadaoka, Suita, Osaka, Japan*
(Received 28 April 2010; revised manuscript received 20 June 2010; published 12 July 2010)

An incipient plastic deformation of several types of grain boundaries subjected to nanoindentation was investigated by atomistic simulations. Our previous study showed that the dislocation nucleation in the inner region of the defect-free metals occurs when the resolved shear stress exceeds a particular stress level slightly higher than the ideal shear strength. However, crystal defects such as grain boundaries undermine the nucleation resistance. In this paper, we examined the dislocation nucleation mechanism at the twin and several coincidence site lattice grain boundaries and the resulting weakening of the dislocation nucleation resistance. We found that for the twin and the relatively stable $\Sigma 11(\bar{1}13)[110]$ grain boundary, the primary slip deformation is activated on the grain-boundary plane prior to the defect-free region because of the low fault energy of the grain boundaries during slip deformation. Subsequently, the secondary slip is activated from the grain boundary. On the other hand, the dislocation is initially generated from the heterogeneous grain-boundary plane for the unstable high-energy grain boundaries.

DOI: 10.1103/PhysRevB.82.024101 PACS number(s): 61.72.Yx, 02.70.Ns, 61.72.Lk, 61.72.Mm

I. INTRODUCTION

Dislocation nucleation is central to the understanding of the initial yield event and plastic deformation as well as the dynamic motion of dislocations. In conventional crystalline metals, dislocations are activated from the preexisting crystal defects such as the Frank-Read source and grain boundaries: the former is the dominant process in the easy glide stage and the latter is important in the post work-hardening stage. Activation from the Frank-Read source occurs when the resolved shear stress exceeds a specific critical value, which depends on the intrinsic lattice resistance known as Peierls stress and the elastic resistance from dislocation line tension.[1,2] In general, it is unlikely that dislocations nucleate homogeneously in the bulk region because of the far higher shear stress being equivalent to the ideal shear strength. However, the homogeneous nucleation of a dislocation occurs when the stress is localized under a concentrated load condition, which is unlike uniaxial tensile testing. Nanoindentation is a typical example of such a boundary condition and a number of experimental studies have indicated that a drastic growth in the indentation displacement arises from the homogeneous nucleation of a large number of dislocations.[3–6] Atomistic simulations have shown that the first dislocation nucleation, as an incipient plastic deformation in a defect-free crystal, occurs in the inner region beneath the indenter.[7–12] Other nucleation events of interest other than the Frank-Read source require an understanding of how dislocations are activated at the grain boundaries. This will lead to an understanding of the post phenomenon of grain-boundary hardening in which a high stress concentration condition is generated by dislocation pile up. Some specific characteristics of grain-boundary dislocation processes are well understood through both experimental observations and computational simulations only focused on the twin boundary. We note that the twin boundary may be a source of dislocations during the initial stage of plastic deformation[13,14] and that the lattice dislocation is dissociated into several partial dislocations at the twin boundary.[15–19] However, there is a need to better understand various grain-boundary characteristics as well as secondary growth behavior at the twin boundary since real polycrystalline materials include a huge variety of grain boundaries. Grain-boundary proximity effects during nanoindentation were studied in a specific coincidence site lattice (CSL) grain-boundary characteristics, and the lowering effect on critical mean pressure equivalent to hardness and slip event in the grain boundary were explained by atomistic simulations.[20,21] In this study, we focused on several symmetric tilt grain boundaries with a CSL including twin and other energetically stable and unstable grain boundaries in copper and performed atomistic simulations of nanoindentation tests on the bicrystal with these grain boundaries. We discuss the dislocation nucleation mechanism at the grain boundaries under the localized stress condition and the weakening effect that depends on the distance between the indentation axis and the grain boundary.

II. ANALYSIS METHOD

In the present study, four symmetrical CSL structures: $\Sigma 3(\bar{1}11)[110]$, $\Sigma 3(\bar{1}12)[110]$, $\Sigma 11(\bar{3}32)[110]$, and $\Sigma 11(\bar{1}13)[110]$ were chosen for bicrystal models, where $\Sigma 3(\bar{1}11)[110]$ is the twin boundary and $\Sigma 11(\bar{1}13)[110]$ is the energetically stable CSL corresponding to a cusp in the grain-boundary energy. The others are unstable CSL grain boundaries. They were constructed by $\langle 110 \rangle$ axial rotations at a specific angle and the triaxial periodic boundary conditions were satisfied. Stable configurations were obtained by finite-temperature molecular dynamics and molecular statics with conjugate gradient (CG) energy minimization, where the fully relaxed configurations were obtained by the CG method when the energy norm of all the atoms converged at 0.01 eV/Å. The atomic interaction was described by the

TABLE I. Grain-boundary energies of twin and three CSL boundaries in Al and Cu evaluated via EAM and DFT.

		Grain-boundary energy (mJ/m^2)			
		$\Sigma3(\bar{1}11)$	$\Sigma3(\bar{1}12)$	$\Sigma11(\bar{3}32)$	$\Sigma11(\bar{1}13)$
Al	EAM	75.1	354.2	496.1	150.5
	DFT-GGA[a]	50.8	331.6	444.6	166.0
Cu	EAM	22.2	586.2	702.7	307.8
	DFT-GGA	12.0	547.0	787.0	284.4

[a]Reference 18.

embedded atom method (EAM) potential, as proposed by Mishin *et al.*[22,23] To evaluate the validity of the employed potential, we compared the results from *ab initio* density-functional theory (DFT) calculations where the DFT calculations were performed as discussed in our previous study.[18] Therefore, we prepared atomic models with 72, 86, 116, and 96 atoms for each grain boundary and used the Vienna *ab initio* simulation package (VASP) (Ref. 24) with the ultrasoft pseudopotential[25] and the Perdew-Wang generalized gradient approximation (GGA) exchange-correlation density functional.[26] The Brillouin-zone k-point samplings were the same as those in Ref. 18 and were chosen using the Monkhorst-Pack algorithm.[27] Grain-boundary fault energies for the four grain boundaries were calculated using EAM and DFT, and are shown in Table I. In this table, we show the case for aluminum by a comparison of the general grain-boundary characteristics. For both copper and aluminum, the grain-boundary energies calculated by the EAM potential accord well with the results from DFT. This table indicates that the grain-boundary energies of aluminum are lower than those of copper except for the twin boundary and this was also found in our preliminary results using EAM for 45 ⟨110⟩ CSL structures from $\Sigma3$ to $\Sigma99$. These tendencies correlate well with the vacancy formation energy and are derived from the electronic binding state, where heterogeneous atomic structures around the grain boundary are stabilized by the directional bonding of aluminum.

An analytical model for nanoindentation simulations is summarized schematically in Fig. 1. A rectangular bicrystal with a CSL grain boundary is prepared. In Fig. 1, the y axis is in the direction normal to the grain boundary, z is equal to the rotation axis, that is ⟨110⟩, and the x axis corresponds to the cross product of the other two axes. Atomistic models of all the CSL structures have dimensions nearly equal to $18 \times 36 \times 18$ nm^3, which are aligned along the above-mentioned directions. The indentation axis for all the CSL models was set in the ⟨110⟩ direction and the elastic resistance under nanoindentation was assumed to be the same for each model. One side of the (110) planes is a traction-free surface on which the indentation was applied, and the atoms located at the bottom were absolutely fixed. Periodic boundary conditions were applied in the direction perpendicular to the indentation axis. The frictionless contact between the atomic models and the spherical indenter is expressed by a repulsive potential.[28] The radius of the indenter was 15 nm, and we confirmed that the dislocations were homogeneously nucleated in the inner region under the indenter with the above-mentioned radius.[9] A quasistatic analysis at absolute zero temperature is generally performed by the CG method. The indent load is applied iteratively by small increments of 0.02 nm of the indent displacement, and a fully relaxed configuration for a given displacement is gradually optimized after sufficient relaxation steps in the CG method until the convergence condition meets the given value, which in our case was when the normalized potential energy gradient for all degrees of configuration freedom drops to below 0.05 eV/Å. The CG relaxations are reiterated until the indent depth reached a maximum depth (1.5 nm). Therefore, a series of calculations were performed on the four bicrystal models and five different indented positions were created for each CSL by changing the distances a between the grain boundaries and the indentation axis, where a was set to 0, 1, 2, 4, and 8 nm, as shown in Fig. 1.

III. RESULTS AND DISCUSSION

The indent load-displacement curves of four CSLs and five positions for each CSL are summarized in Fig. 2. For the single crystal under the (110) indentation, a Hertzian elastic solution[29] expressed by $P=(4/3)E^*R^{1/2}h^{3/2}$ is shown in these figures. R is the radius of the spherical indenter, h is the indentation displacement, and E^* is the reduced indentation modulus represented by the Young's modulus and the Poisson's ratio of the specimen and indenter. In these simula-

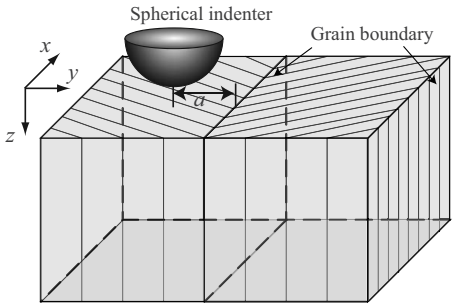

FIG. 1. Schematic of nanoindentation on bicrystals. Four energetically stable and unstable grain boundaries were placed in the direction perpendicular to the x axis, and the indentation was implemented at a position a nm away from one side of boundary.

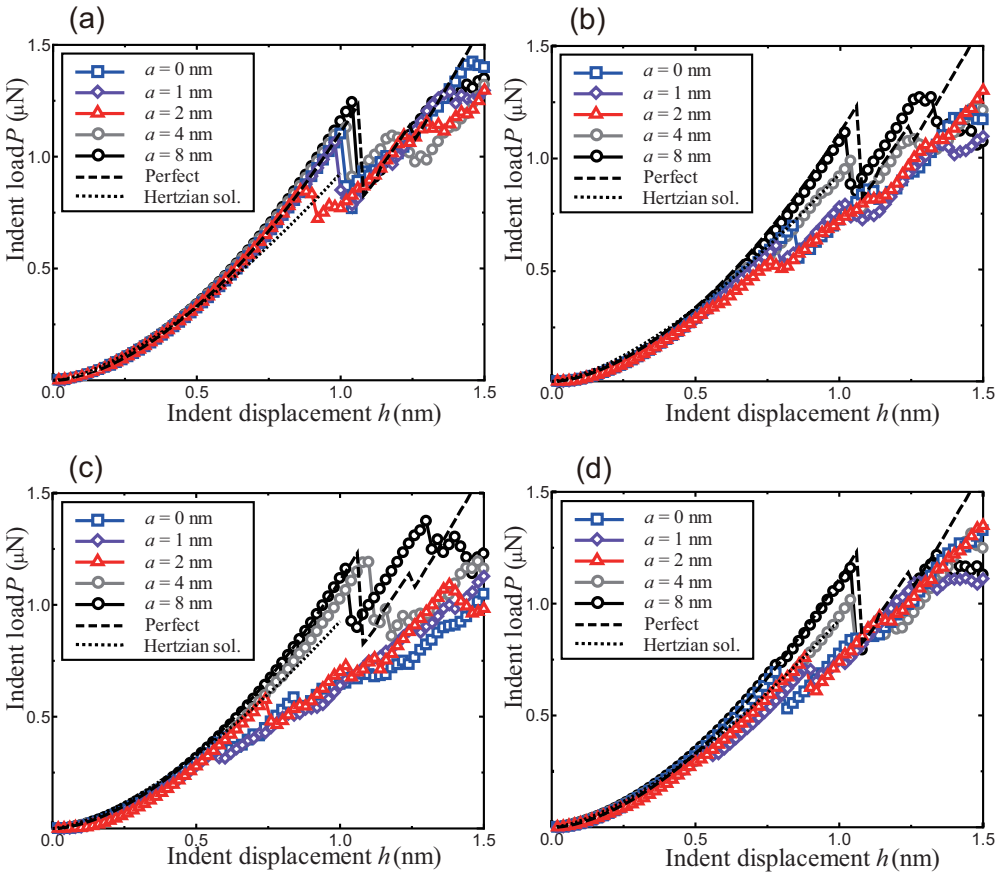

FIG. 2. (Color online) Relationships between indent load and indent displacement which indicates differences in distance between the indentation axis and the grain boundary indented on the four bicrystals (a) $\Sigma3(\bar{1}11)$, (b) $\Sigma3(\bar{1}12)$, (c) $\Sigma11(\bar{3}32)$, and (d) $\Sigma11(\bar{1}13)$.

tions, a virtual frictionless and rigid indenter was used and the reduced modulus is given by $E^*=E'/(1-\nu')$. On the assumption that the tentative isotropic elastic properties can be evaluated via the Voigt average of the uniaxially assumed Young's modulus $E'=(C_{11}-C_{12})(C_{11}+2C_{12})/(C_{11}+C_{12})$ and Poisson's ratio $\nu'=C_{12}/(C_{11}+C_{12})$ by employing the direction cosine of anisotropic elastic constants,[18] coefficients for the (110) indentation are given as follows: $E'=163$ GPa, $\nu'=0.302$, and $E^*=179$ GPa. Figure 2 shows that the elastic response can be reproduced well by the Hertzian solution with the Voigt average even in the case of strongly anisotropic copper. The load drops that are observed after continuous elastic deformation in all the bicrystals correspond to dislocation nucleation and the critical values for each bicrystal are smaller than that of a single crystal. As shown in our previous study, the critical mean pressure p_c, which is obtained by the indent load divided by the contact area is one of the most important indicators of dislocation nucleation because the relationship between the maximum shear stress and the mean pressure is linear even in anisotropic media. The dependence on the converted critical mean pressures from the distance between the grain boundary and the indentation axis are summarized in Fig. 3. Compared to the single crystal, the critical mean pressures of the bicrystals decrease when the indentation tests are applied near the grain boundaries. The grain boundaries have little influence on the value at a distance of 8.0 nm from the grain boundaries. Additionally, the decrease at a distance of 1.0 or 2.0 nm is more apparent than that directly on the grain boundary since the maximum shear stress is generated at a slight distance from the indentation axis, which is derived from the anisotropy of the media.[18] The minimum values of the critical pressure for all the bicrystals are 10.8, 7.7, 6.6, and 8.8 GPa in $\Sigma3(\bar{1}11)$, $\Sigma3(\bar{1}12)$, $\Sigma11(\bar{3}32)$, and $\Sigma11(\bar{1}13)$, respectively. These values indicate that the decrease in the critical mean pressure

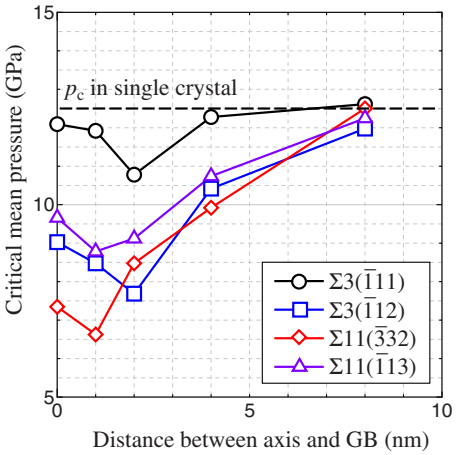

FIG. 3. (Color online) Critical mean pressure in relation to the distance between the axis and the grain boundary for each bicrystal.

correlates with the grain-boundary energy although the distance between the position of maximum shear stress and the grain boundary deserves close attention. The Schmid factor in the ⟨110⟩ tension is 0.408 and this is the same for all the bicrystal models.

Dislocation nucleation under the nanoindentation of a single crystal occurs when the resolved shear stress reaches an ideal shear strength under triaxial compressive stress and subsequently the surface steps generated by dislocation dipoles induce the first load drop.[30] Here, we consider the nucleation mechanism of dislocation in bicrystals. When focusing on $\Sigma3(\bar{1}11)$, it is expected from the low boundary energy that the $\Sigma3(\bar{1}11)$ twin boundary is much more coherent than the other grain boundaries and that it shows bulklike characteristics under deformation. As shown in Fig. 2, however, the critical pressure of the $\Sigma3(\bar{1}11)$ bicrystal drops to 84.3% compared with the single crystal, and thus the yield mechanism under deformation, other than the static properties, still needs to be established. We implemented the nudged elastic band (NEB) method[31] with parallel computation techniques to investigate the transition state between the elastic deformation stage and the initial yield stage. The initial and final states were chosen to extract the $\Sigma3(\bar{1}11)$ bicrystal indented 2 nm from the boundary just before and after the initial yield event. Atomic images[32] of the transition states after the fully relaxed NEB steps are shown in Fig. 4(a) where the defect structures include surface, grain boundaries, and the dislocation and are visualized using a centrosymmetry parameter.[28] We found that the initial yield event corresponding to the dislocation emission occurs directly on the twin boundary plane [see Fig. 4(a)(B)]. From a crystallographic perspective as shown in Fig. 4(b), the Burgers vector of this glide dislocation on the twin boundary was found to be $(1/6)a_0[211](D\beta)$, and it fits the definition of a displacement site lattice (DSC) dislocation, which is defined as the minimum unit of the parallel displacement on the boundary. Here a_0 is the lattice constant and is equal to 3.615 Å for the adopted interatomic potential. After DSC dislocation gliding, the boundary plane shifts with the magnitude of the vector $(1/3)a_0[\bar{1}11]$ and is perpendicular to the twin boundary. Subsequently, a glide dislocation is emitted from part of the DSC dislocation and the Burgers vector of the dislocation is $(1/2)a_0[011](DB)$ and this dissociates into $(1/6)a_0[121](D\alpha)$ and $(1/6)a_0[\bar{1}12](\alpha B)$ on the $(1\bar{1}1)$ slip plane. It is not until the glide dislocation reaches the interface between the indenter and the surface that a load drop is observed. This finding supports our previous conclusion with respect to the abrupt increase in indent displacement observed in general nanoindentation experiments. The incipient plastic deformation is triggered by surface steps corresponding to the dislocation dipoles. It is noted that creating an intrinsic stacking fault or a twin fault is equivalent to nucleating a Shockley partial or twinning dislocation with $b_s = (\sqrt{6}/6)a_0$ and therefore the energy barrier for each faulting should dominate the slip deformation mode.[33] The fault energies of both the perfect crystal and the bicrystal of the twin and other CSL grain boundaries along the minimum-energy direction as a function of the rigid displacements are shown in Fig. 5, where atomic displacement in the direction perpendicular to the grain-boundary plane is fixed. The normal glide plane of the perfect crystal is an arbitrary {111} plane and the curve for the perfect crystal is known as the generalized stacking-fault energy. The direction of displacements of the twin bicrystals corresponds to the DSC direction, and

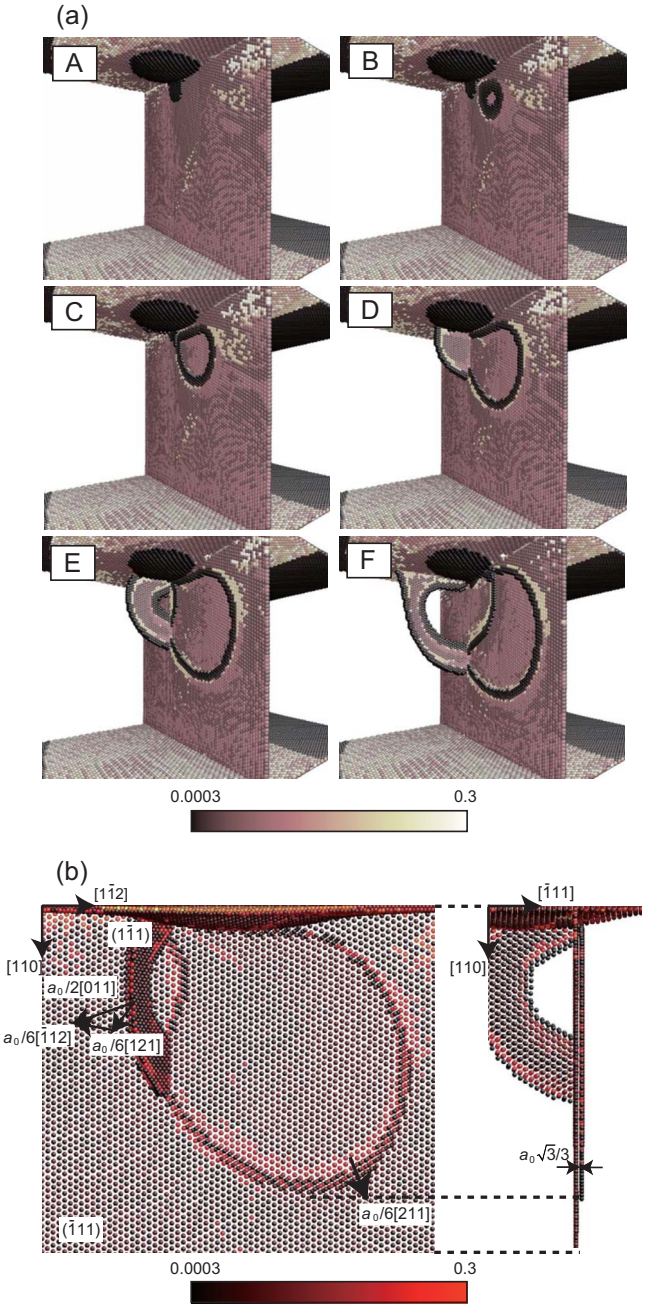

FIG. 4. (Color online) Atomic images for the initial yield event obtained by NEB analysis, where atoms are visualized according to the centrosymmetry parameter with the parameter range between 0.0003 and 0.3. (a) The initial and final states corresponding to before and after the load drop are shown in (a) and (f), respectively, and the transition states between the initial and final states are shown by (b)–(e). (b) Crystallographic orientation of the displacement site lattice dislocation on the twin boundary and the slip dislocation.

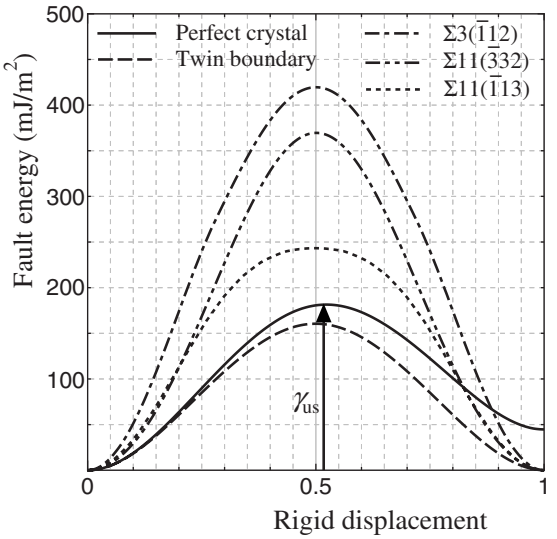

FIG. 5. Fault energies of the bicrystals along the minimum-energy direction as a function of the rigid displacement in comparison with the generalized stacking-fault energy. Displacements are normalized by the unit lengths of DSC lattice dislocation $(\sqrt{6}/6)a_0$ in twin boundary and the periodic lattice in the $\langle 110 \rangle$ direction of fcc crystal $(\sqrt{2}/2)a_0$ in other types of grain boundaries.

those of the other bicrystals correspond to the $\langle 110 \rangle$ directions. The unstable stacking-fault energy and the fault energy of the twin boundary are 181.4 $\mathrm{mJ/m^2}$ and 160.1 $\mathrm{mJ/m^2}$, respectively. We found that the fault energy of the twin boundary is lower than the unstable stacking-fault energy and, therefore, despite their similar crystallographic orientations in a perfect crystal and the twin boundary, the DSC dislocation on the twin boundary is emitted before homogeneous dislocation nucleation in the bulk region. The nucleation mechanism of the dislocations, other than for the twin boundary, is shown in Figs. 6(a)–6(c). In unstable grain boundaries such as $\Sigma 3(\bar{1}12)$ and $\Sigma 11(\bar{3}32)$, dislocations are initially activated in the heterogeneous region and then move to the inner region. On the other hand, grain-boundary sliding occurs and then glide dislocations are emitted from a part of the sliding grain in the case of the relatively stable $\Sigma 11(\bar{1}13)$. The direction of grain-boundary sliding is $\langle 110 \rangle$, which is consistent with the minimum-energy direction. In this study, the indentation was implemented on the (110) plane and, therefore, a higher order of shear stress is inevitably generated, as shown in Fig. 6(d). Each atom is color coded according to the shear stress τ_{zx} normalized in the range $-5.0 \leq \tau_{zx} \leq 5.0$ GPa. Grain-boundary sliding is induced in preference to the dislocation emission when that the fault energy is not high compared with the unstable stacking-fault energy. The resolved shear stress along the $\langle 110 \rangle$ directional minimum-energy path for sliding has a significant effect. Therefore, the incipient yield processes occur more easily than dislocation nucleation within the bulk region with accompanying grain-boundary sliding and interface activation and they have a significant correlation with the inherent grain-boundary stability and fault energy of grain-boundary sliding.

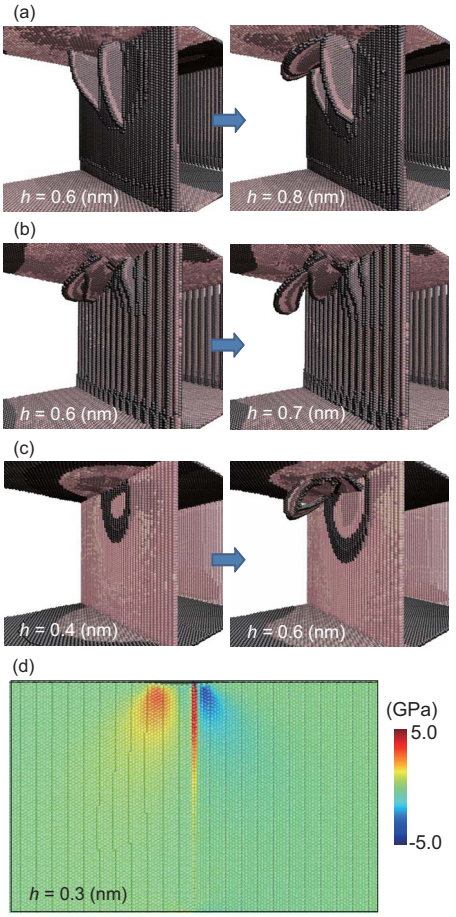

FIG. 6. (Color online) Dislocation nucleation of bicrystals except for the twin boundary, which include the (a) $\Sigma 3(\bar{1}12)$, (b) $\Sigma 11(\bar{3}32)$, and (c) $\Sigma 11(\bar{1}13)$ grain boundaries. (d) Stress distribution of the τ_{zx} component in the case of $\Sigma 11(\bar{1}13)$ bicrystal.

IV. SUMMARY

In summary, dislocation nucleation at the twin boundary and several stable/unstable CSL grain boundaries during the nanoindentation of bicrystals were investigated by atomistic simulations. Although incipient yield events in all the bicrystals occur at a lower indent load than for a perfect crystal, the yield mechanisms vary considerably for the different grain boundaries. A twin boundary DSC lattice dislocation on the boundary is emitted before shear loop nucleation in the bulk because of the lower fault energy of the grain-boundary sliding rather than stacking-fault energy. In addition to the twin boundary, grain-boundary sliding is induced in the stable $\Sigma 11(\bar{1}13)$ grain boundary only if the in-plane direction of the shear stress is along a particular $\langle 110 \rangle$ direction. On the other hand, dislocations are readily activated on the grain-boundary plane in the other unstable grain boundaries $\Sigma 3(\bar{1}12)$ and $\Sigma 11(\bar{3}32)$ with much higher fault energies and local stress concentrations. These mechanisms of dislocation nucleation are strongly associated with the static grain-boundary stability and fault energy for grain-boundary sliding.

ACKNOWLEDGMENTS

The authors T.T. and Y.S. acknowledge recurring financial support from the Japan Society for the Promotion of Science (JSPS), Grant-in-Aid for Young Scientists (B, Grant No. 21760090) (T.T.) and Grants-in-Aid for Scientific Research (S, Grant No. 20226004) (Y.S.). Technical support for parallel computing from the Center for Computational Science and e-Systems at the Japan Atomic Energy Agency is appreciated.

[1] H. M. Zbib, M. Rhee, and J. P. Hirth, Int. J. Mech. Sci. **40**, 113 (1998).
[2] B. Devincre, L. Kubin, C. Lemarchand, and R. Madec, Mater. Sci. Eng., A **309-310**, 211 (2001).
[3] W. W. Gerberich, J. C. Nelson, E. T. Lilleodden, P. Anderson, and J. T. Wyrobek, Acta Mater. **44**, 3585 (1996).
[4] S. Suresh, T. G. Nieh, and B. W. Choi, Scr. Mater. **41**, 951 (1999).
[5] Y. Shibutani, T. Tsuru, and A. Koyama, Acta Mater. **55**, 1813 (2007).
[6] D. Lorenz, A. Zeckzer, U. Hilpert, P. Grau, H. Johansen, and H. S. Leipner, Phys. Rev. B **67**, 172101 (2003).
[7] A. Gouldstone, K. J. Van Vliet, and S. Suresh, Nature (London) **411**, 656 (2001).
[8] A. Gannepalli and S. K. Mallapragada, Phys. Rev. B **66**, 104103 (2002).
[9] T. Tsuru and Y. Shibutani, Phys. Rev. B **75**, 035415 (2007).
[10] X. H. Liu, J. F. Gu, Y. Shen, and C. F. Chen, Scr. Mater. **58**, 564 (2008).
[11] R. J. Wagner, L. Ma, F. Tavazza, and L. E. Levine, J. Appl. Phys. **104**, 114311 (2008).
[12] V. Navarro, O. R. de la Fuente, A. Mascaraque, and J. M. Rojo, Phys. Rev. Lett. **100**, 105504 (2008).
[13] J. E. Flinn, D. P. Field, G. E. Korth, T. M. Lillo, and J. Macheret, Acta Mater. **49**, 2065 (2001).
[14] D. P. Field, B. W. True, T. M. Lillo, and J. E. Flinn, Mater. Sci. Eng., A **372**, 173 (2004).
[15] C. Solenthaler, Mater. Sci. Eng., A **125**, 57 (1990).
[16] Z. Chen, Z. Jin, and H. Gao, Phys. Rev. B **75**, 212104 (2007).
[17] Z. H. Jin, P. Gumbsch, K. Albe, E. Ma, K. Lu, H. Gleiter, and H. Hahn, Acta Mater. **56**, 1126 (2008).
[18] T. Tsuru, Y. Shibutani, and Y. Kaji, Phys. Rev. B **79**, 012104 (2009).
[19] C. Deng and F. Sansoz, Acta Mater. **57**, 6090 (2009).
[20] E. T. Lilleodden, J. A. Zimmerman, S. M. Foiles, and W. D. Nix, J. Mech. Phys. Solids **51**, 901 (2003).
[21] D. Saraev and R. E. Miller, Modell. Simul. Mater. Sci. Eng. **13**, 1089 (2005).
[22] Y. Mishin, D. Farkas, M. J. Mehl, and D. A. Papaconstantopoulos, Phys. Rev. B **59**, 3393 (1999).
[23] Y. Mishin, M. J. Mehl, D. A. Papaconstantopoulos, A. F. Voter, and J. D. Kress, Phys. Rev. B **63**, 224106 (2001).
[24] G. Kresse and J. Hafner, Phys. Rev. B **47**, 558 (1993).
[25] G. Kresse and J. Furthmuller, Phys. Rev. B **54**, 11169 (1996).
[26] J. P. Perdew, J. A. Chevary, S. H. Vosko, K. A. Jackson, M. R. Pederson, D. J. Singh, and C. Fiolhais, Phys. Rev. B **46**, 6671 (1992).
[27] H. J. Monkhorst and J. D. Pack, Phys. Rev. B **13**, 5188 (1976).
[28] C. L. Kelchner, S. J. Plimpton, and J. C. Hamilton, Phys. Rev. B **58**, 11085 (1998).
[29] K. L. Johnson, *Contacts Mechanics* (Cambridge University Press, Cambridge, 2003).
[30] T. Tsuru, Y. Shibutani, and Y. Kaji, Acta Mater. **58**, 3096 (2010).
[31] G. Henkelman, B. P. Uberuaga, and H. Jónsson, J. Chem. Phys. **113**, 9901 (2000).
[32] J. Li, Modell. Simul. Mater. Sci. Eng. **11**, 173 (2003).
[33] Z. H. Jin, P. Gumbsch, E. Ma, K. Albe, K. Lu, H. Hahn, and H. Gleiter, Scr. Mater. **54**, 1163 (2006).